Interaction between gravity-driven listric normal fault linkage and their hanging-wall rollover development: a case study from the western Niger Delta, Nigeria

HAMED FAZLIKHANI[1]*, STEFAN BACK[2], PETER A. KUKLA[2] & HAAKON FOSSEN[1,3]

[1]*Department of Earth Science, University of Bergen, Postboks 7803, 5007 Bergen, Norway*

[2]*Geological Institute, EMR, RWTH Aachen University, 52062 Aachen, Germany*

[3]*Museum of Natural History, University of Bergen, Postboks 7803, 5007 Bergen, Norway*

**Correspondence: hamed.khani@uib.no*

Abstract: Rollover is the folding of the hanging-wall sedimentary record in response to slip on listric normal faults, and is a common feature of sediment-rich, gravity-driven tectonic provinces. Rollovers have been extensively studied by means of geometrical reconstruction, and numerical and analogue modelling. However, the detailed interaction between the kinematics of bounding listric normal faults and their hanging-wall deformation is not yet fully understood. In this study, we use 3D seismic-reflection data from the Forcados-Yokri area, western Niger Delta, Nigeria, to study the lateral linkage and landwards backstepping history of an array of listric normal faults, particularly focusing on their influence on the development and evolution of hanging-wall rollovers. Five individual, partly overlapping rollover structures have been studied with respect to their relative initiation and decay time, their spatial distribution, and their relationship to the tectonic history of their respective bounding faults. We demonstrate that the studied rollovers are highly dependent on the development of their bounding faults in terms of initiation time, lateral linkage, internal structural development and decay. Fault–rollover interaction is dynamic and changes through time depending on the temporal evolution of listric faults. Four genetic types of fault–rollover interaction were identified in this study: (1) the rotation of a rollover–crestal-collapse system, controlled by a changing lateral bounding-fault orientation during fault growth; (2) a stepwise shift of rollover–crestal-collapse systems associated with rollover abandonment, controlled by the initiation of a new fault in the footwall of an older structure; (3) a gradual shift of successive rollovers controlled by branching main faults; and (4) a general landwards and upwards migration of crestal-collapse faults within a rollover above stationary listric main faults.

Listric normal faults are characteristic of gravity-driven thin-skinned structural domains, including the Niger Delta (e.g. Doust & Omatsola 1989; Dula 1991; Morley & Guerin 1996; Rouby & Cobbold 1996; Hooper *et al.* 2002; Back *et al.* 2006; Fazli Khani & Back 2012; Sapin *et al.* 2012), the Nile Delta (e.g. Sestini 1989; Beach & Trayner 1991; Marten *et al.* 2004), the Mahakam Delta (e.g. Dooley *et al.* 2000), the Baram Delta province of NW Borneo (e.g. Sandal 1996; Van Rensbergen & Morley 2000; Hodgetts *et al.* 2001; Imber *et al.* 2003; Morley *et al.* 2003; Saller & Blake 2003; Back *et al.* 2005, 2008; Sapin *et al.* 2012) and the Gulf of Mexico (e.g. Lopez 1990; Cartwright *et al.* 1998; Brown *et al.* 2004; Shen *et al.* 2016). Deposition of denser sediments, mainly sandstones above water-saturated shales or evaporites (weaker substratum), create a gravitational instability that is commonly accommodated by synsedimentary normal faults (Thorsen 1963; Bruce 1973; Edwards 1976; Lowell 1985; McCulloh 1988; Morley & Guerin 1996; Rouby & Cobbold 1996; Van Rensbergen & Morley 2000; Back & Morley 2016). Space created by the initiation of normal faults will be filled continuously by sediments (Fazli Khani & Back 2015*a*), and the additional load represented by these sediments helps to maintain slip on the fault. Progressive slip on the listric fault usually triggers the initiation of a rollover anticline in the hanging-wall domain (Gibbs 1984; Xiao & Suppe 1992; Mauduit & Brun 1998). Rollover anticlines and associated crestal-collapse faults can thus be interpreted as the consequence of stratal bending due to slip along listric normal faults with synchronous sedimentation. In sediment-rich deltaic settings, the synkinematic sedimentary record of rollovers can therefore preserve, for example, the consequences of lateral fault growth and linkage, changes in the strike of the bounding fault or the decay of slip along growth faults through time. The interaction

From: CHILDS, C., HOLDSWORTH, R. E., JACKSON, C. A.-L., MANZOCCHI, T., WALSH, J. J. & YIELDING, G. (eds) *The Geometry and Growth of Normal Faults*. Geological Society, London, Special Publications, **439**, https://doi.org/10.1144/SP439.20

between a listric normal fault and its hanging-wall rollover has been demonstrated by analogue modelling (e.g. Ellis & McClay 1988; Vendeville & Cobbold 1988; McClay 1990; Withjack *et al.* 1995; Withjack & Schlische 2006), numerical modelling (White *et al*. 1986; Xiao & Suppe 1992; Ings & Beaumont 2010) and by 3D seismic interpretation (Hodgetts *et al.* 2001; Imber *et al.* 2003; Back *et al.* 2006; Pochat *et al*. 2009; Fazli Khani & Back 2012, 2015*a*). The study of Imber *et al.* (2003) on a listric growth-fault system from SE Asia is particularly important in that it demonstrates in one part of their study area a prolonged and progressive landwards migration of active rollover in the hanging wall of a stationary main fault, while in another there is a punctuated migration directly related to the stepping of the bounding fault. Fazli Khani & Back (2012) documented a similar dynamic rollover development tied to bounding-fault migration in the Niger Delta, highlighting the landwards rollover migration and complexities in a system affected by coinciding seawards and landwards fault migration. This study (using the same dataset described by Fazli Khani & Back 2012, 2015*a*, *b*) focuses on a detailed analysis of the migration, lateral linkage and geometrical changes associated with multiple shifting, growing and linking bounding faults that affect the development of several adjacent, partly overlapping rollovers. We present, as examples, five coupled growth-fault rollover systems that have been identified on 3D seismic-reflection data from the western Niger Delta (Fig. 1). In these systems, bounding-fault growth and linkage can be documented by fault-kinematic analysis (throw–distance and throw–depth plots) and analysis of time–thickness maps. These data are subsequently analysed with respect to the development of the associated rollover and crestal-collapse systems, documenting significant diversity between neighbouring, partly contemporaneous, detaic rollovers.

Geological framework

The Niger Delta is one of the Earth's largest Cenozoic delta systems. It formed during the separation of South America from Africa during Early Cretaceous times (Whiteman 1982; Fairhead & Binks 1991). It is located on the West African continental margin at the apex of the Gulf of Guinea (Fig. 1a). Deltaic sedimentation started during the Late Eocene (Burke 1972; Whiteman 1982; Damuth 1994) at the SW (seawards) edge of the Benue Trough. The delta succession comprises a highly progradational, generally upwards-coarsening association of Cenozoic clastics up to 12 km thick (Doust & Omatsola 1989). The Niger Delta lithostratighraphy is subdivided into three major units from the Paleocene to recent in age, comprising: (1) basal marine pro-delta shales of the Akata Formation; (2) sandstone-rich paralic siliciclastics of delta-front, delta-topset and fluvio-deltaic environments of the Agbada Formation; and (3) alluvial and upper coastal plain sandstones of the Benin Formation (Fig. 1b) (cf. Short & Staeuble 1967; Evamy *et al.* 1978; Whiteman 1982). The delta stratigraphy and structure are intimately related, with the development of each being dependent on the interplay between sediment supply and subsidence (Doust 1990). The study area is located in the extensional, gravity-driven coastal structural domain of the delta (Fig. 1a, c), in which the progradation of the deltaic sedimentary wedge over basal marine shales caused the formation of numerous kilometre-scale synsedimentary growth faults (Fig. 1b) (Doust & Omatsola 1989; Damuth 1994; Hooper *et al.* 2002).

Figure 1c shows an example of a horizon slice that highlights the occurrence of faults in the study area, emphasizing a series of major arcuate-shaped, seawards-dipping, normal deltaic faults that are, in places, associated with hanging-wall rollovers. The NW part of the study area is characterized by several arcuate-shaped normal faults that extend laterally over several kilometres (Table 1), dividing the area into four fault blocks (Fig. 1c). In contrast, the central and SE parts of the study area are characterized by deltaic rollovers with collapsed crests that are bound on the landwards side by a series of sub-parallel, seawards-dipping, listric growth faults (Fig. 2). On the seawards side, the rollover province is bound by a large, slightly listric, seawards-dipping fault system (SE segment of fault F1: Fig. 2). The vertical seismic sections of Figure 2 illustrate the relationships between the fault architecture, the hanging-wall rollover geometries and the syntectonic stratigraphic record. All major bounding faults in the study area show a synsedimentary growth signature: that is, they comprise thickened or additional sedimentary units on their respective downthrown sides.

Datasets and methods

The 3D seismic-reflection data used for this study are from the uppermost 4 km of an approximately 400 km^2 survey area in the coastal zone of the western Niger Delta (Fig. 1). The seismic-reflection data have been processed using pre-stack time migration, and are in European zero-phase polarity convention (i.e. a downwards increase in acoustic impedance corresponds to a seismic trough, which is indicated in red in the colour figures in this paper). Variance attribute volumes were derived from the reflectivity data using a semblance algorithm that highlights lateral amplitude variations between adjacent seismic traces (e.g. Fig. 1c). Detailed mapping and analysis

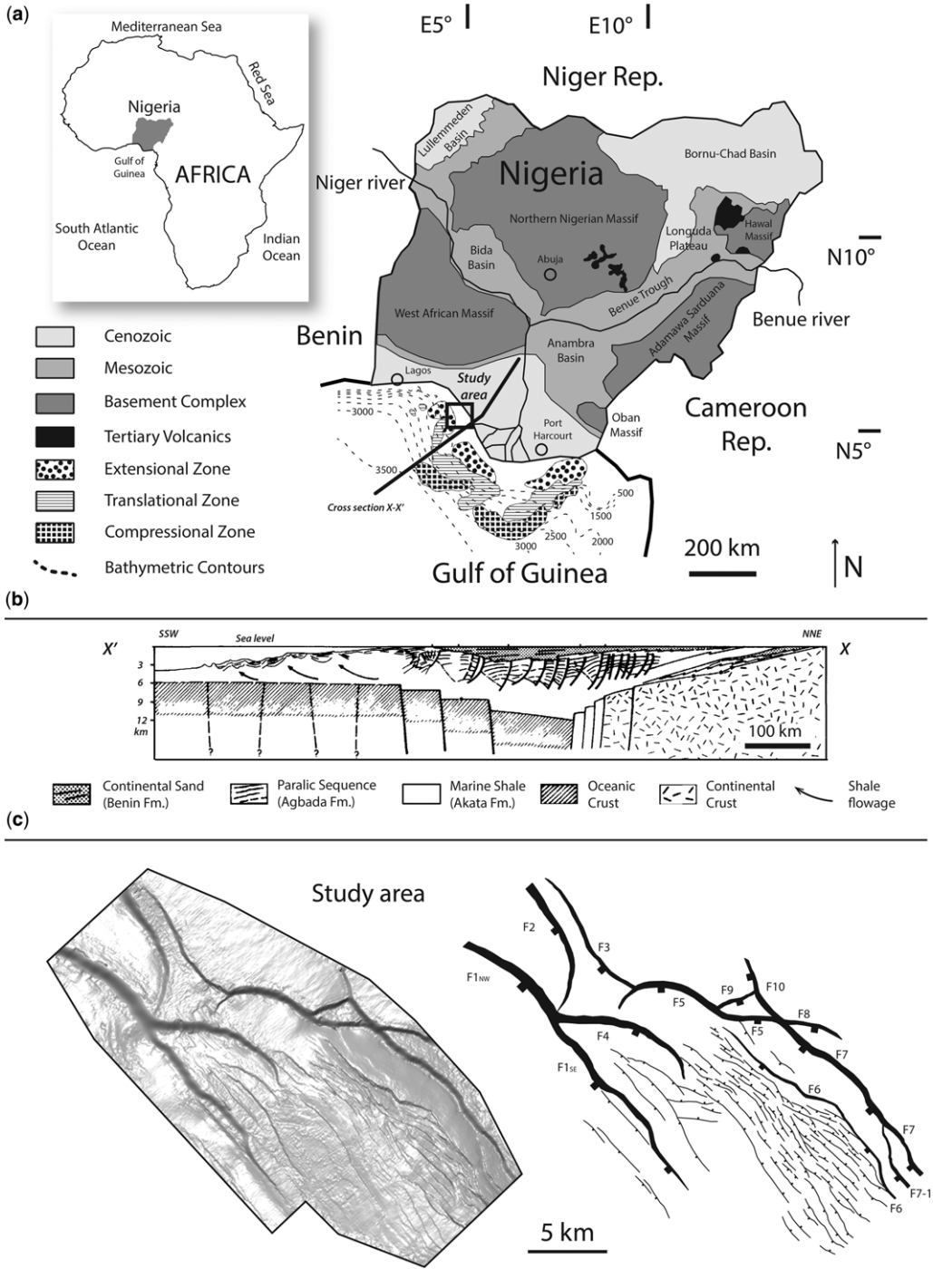

Fig. 1. (**a**) Location and the major onshore geological units (based on Onuoha 1999) of the study area in the western offshore, Niger Delta in Nigeria (offshore gravity-tectonic structural styles and bathymetric contours are based on Damuth 1994). (**b**) Regional cross-section in the vicinity of the study area showing the regional stratigraphic units and structural framework of the Niger Delta (based on Evamy *et al.* 1978). (**c**) Time–structural map of the study area highlighting major bounding listric faults (F1–F10) and their hanging-wall crestal-collapse normal faults.

Table 1. *Major bounding-fault characteristics in the study area*

Fault name	Strike	Dipping towards	Length (at horizon D) (km)	Maximum throw (ms)	Location of maximum throw
Fault 3 (F3)	NW–SE	SW	8	250	Close to the linkage point
Fault 5 (F5)	East–west	South	11	700	At the centre of the fault
Fault 7 (F7)	NW–SE	SW	15	950	Close to the linkage point
Fault 8 (F8)	East–west	South	3.5 (in the study area)	400	Close to the linkage point
Fault 9 (F9)	ENE–WSW	South	3	500	At the centre of the fault
Fault 10 (F10)	NW–SE	SW	4.5 (in the study area)	650	Close to the linkage point

of synsedimentary faults in the seismic dataset were based on interpreting a combination of vertical seismic sections of varying orientation (Fig. 2), together with time and horizon slices in reflectivity and variance display, constructing time–thickness maps, conducting detailed fault-kinematic analyses based on throw–depth plots that show the temporal evolution of faults, and throw–distance plots that show their spatial evolution.

Fault throw measured in milliseconds for two-way travel time (ms TWT) v. depth and distance plots (Fig. 3), and fault-throw v. distance plots (Fig. 4), were constructed from hanging-wall and footwall cut-offs of all interpreted horizons mapped on several orthogonal sections along the strike of all main bounding faults. Compaction of sediments may cause a loss of displacement of up to 15% in the sand or mixed sand–shale successions, with growth indices of greater than approximately 0.1; decompaction is not necessarily required to decipher first-order displacements and fault-growth histories (Taylor *et al.* 2008). Throw–depth plots (Fig. 3) (*sensu* Cartwright *et al.* 1998; Back *et al.* 2006; Hongxing & Anderson 2007; Baudon & Cartwright 2008; Jackson & Rotevatn 2013) illustrate the growth periods of faults, and incremental throw in any given interval can be readily determined from the plot, as can the displacement gradient for any interval. Throw–distance plots (Fig. 4), in turn, illustrate the lateral growth and linkage of fault systems. A single isolated fault has maximum throw at its centre, decreasing laterally towards the fault tips. Complex shapes of the throw–distance curve can be observed, for example, in relay ramp areas with steep throw gradients, or at the location of fault-segment linkage with throw minima (Peacock & Sanderson 1991; Gawthorpe & Leeder 2000; Duffy *et al.* 2015; Fossen & Rotevatn 2016).

Main bounding faults

This study focuses on 10 listric normal faults in the SE part of the studied dataset that bound the major rollover province of the SE to central study area, labelled as faults F1–F10 (Figs 1c & 2). The faults F5, F7, F8 and F10 meet at a common intersection area (Figs 1c & 2), while F9 is oblique to F5 and F10 connects these two faults. The major first-order faults F5 and F7 are arcuate in map view, bounding the dominant rollover anticline in their hanging wall in the centre of the study area (Fig. 2). Faults F8, F9 and F10 are located in the footwall of F5 and F7 at the western edge of the study area.

F3 strikes NW–SE over 8 km and dips towards SW (Table 1; Fig. 2). To the SE, F3 links to F5 and dies out towards the NW. The maximum of throw of 290 ms is measured close to the linkage area with F5 (Fig. 3, plot B), decreasing towards the NW. F5 strikes generally east–west, with dips towards the south. It extends over 11 km at mapped Horizon D (Table 1; Fig. 2). Towards the NW, F5 links to F3 before terminating in the footwall of F4 (Figs 2 & 3). Along-strike throw measurements (throw–distance plot: Fig. 4) show a major decrease in throw at the location of the linkage between F5 and F3. F5 strikes NW–SE in its central part; at the linkage area to F9, it rotates toward the east, trending west–east towards the intersection area indicated in Figure 2. At the location of linkage to F9, a distinct decrease in throw is observed on the throw–distance plot of F5 (Fig. 4). F5 links to F7, F8 and F10 in the intersection area. Fault 9 strikes ENE–WSW over 3 km, and links to F10 towards the NE and to F5 towards the SW (Fig. 2). Fault 10 is located on the western edge of study area in the footwall of F5, over 4.5 km in length (Fig. 2; Table 1). This fault strikes NW–SE from the intersection area, marking its SE tip towards the NW. The NW tip of this fault is located beyond the extent of the study area. Fault 8 is located in the footwall of F7, striking east–west from the intersection area. This fault is about 3.5 km long in the study area (Fig. 2), with a maximum throw of 400 ms measured at the eastern end of fault close to the edge of the study area (Fig. 2; Table 1).

Relative timing of fault initiation and temporal evolution

The throw–depth plots of Figure 3 show the nature and the kinematics of the main bounding faults.

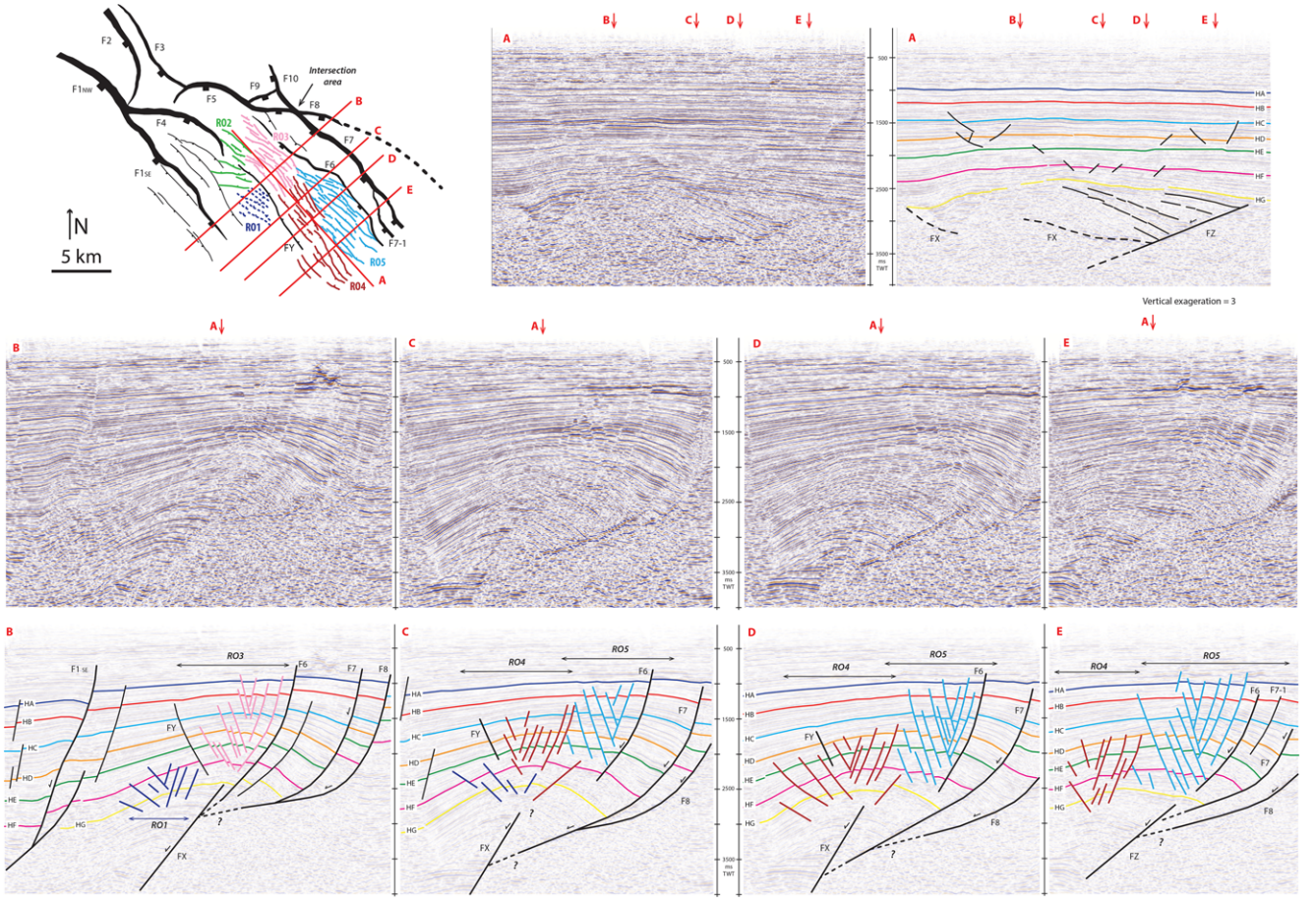

Fig. 2. Structural map at Horizon D and five vertical cross-sections illustrating major structural elements and rollover anticlines in the centre of the study area. Seven horizons have been mapped in the study area and are shown in the vertical time sections (ms, millisecond; TWT, two-way travel time). These horizons are labelled HA–HG from shallow to deeper parts and are the basis for fault kinematics analysis. The dotted line on the map view shows the extension of F8 beyond the study area. Note that cross-section A is perpendicular to sections B, C, D and E. Red arrows show the intersection locations.

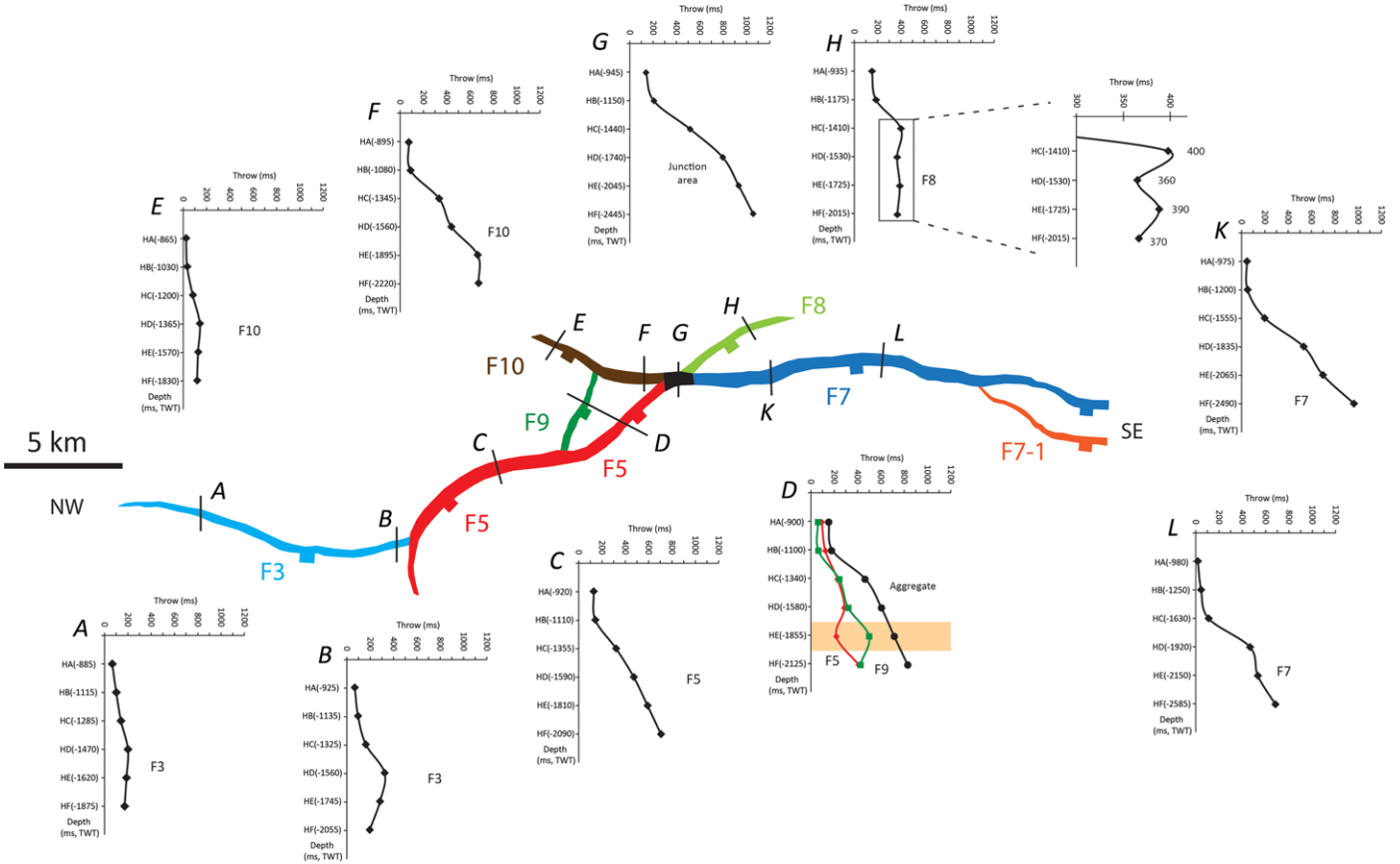

Fig. 3. Throw–depth profiles reflecting the growth of the studied faults. F3 shows rather isolated fault growth characteristics with the maximum throw at Horizon D decreasing both upwards and downwards (plots A and B). F5 and F7 are synsedimentary growth faults with the maximum of throw at Horizon F decreasing upwards in the shallower horizons. Profile D shows the influence of the initiation of F9 in the footwall of F5 (shaded rectangle; orange in the online version). When F9 initiates, a major amount of strain accumulates at Horizon E, causing a throw minima on F5. The graph on the right in plot D shows the aggregate of throw on both F5 and F9, following the same trend as plot C. Profiles E and F show differential fault activity along the strike of F10, highlighting the lateral (towards the north) decrease in fault activity. The vertical scale in brackets is the mid-point between the hanging-wall and footwall cut-offs.

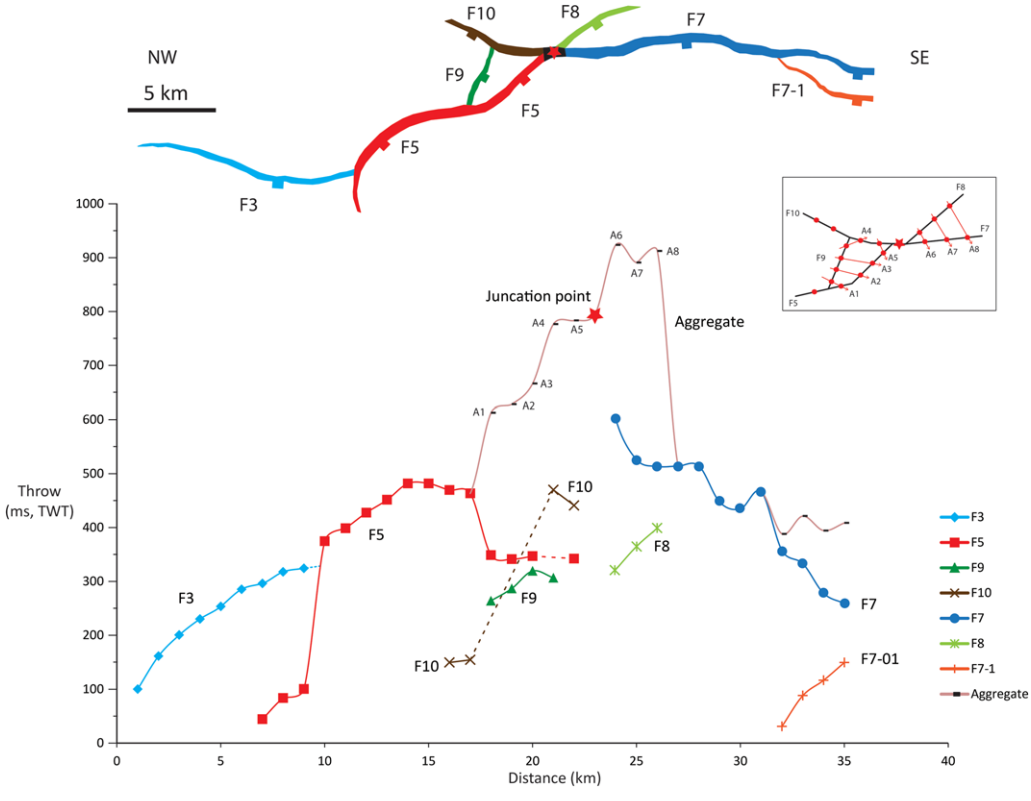

Fig. 4. Throw–distance (T–D) graph showing lateral growth and linkage along the strike of studied bounding faults from NW to SE. This graph is based on the hanging-wall and footwall cut-offs of interpreted Horizon D. Horizon D is the deepest horizon in which we were able to construct throw–distance graphs that show the lateral linkage of studied faults. The aggregated graph shows the amount of throw at and around the relay zone, and is based on the totalled up throw at different measuring points. The inset box shows how the amount of throw was measured in the relay zone in the footwall of F5 to construct the aggregate graph.

From NW to SE, plots A and B show a vertical decrease in throw along the length of F3 close to its NW and SE tips, respectively (Fig. 3). The maximum throw of F3 occurs at Horizon D in both plots A (about 320 ms TWT) and B (about 200 ms TWT), decreasing both upwards and downwards. This suggests that F3 initiated at Horizon D. The magnitude of the throw on F3 decreases towards the NW from the area of linkage towards F5 at its SE tip (see the variation in lateral throw at Horizon D in plots A and B in Fig. 3). This suggests that F3 propagated from the SE towards the NW, consistent with its throw–distance plot in Figure 4.

Plot C of Figure 3 shows the variation in vertical throw in the central portion of F5, with a maximum throw of 830 ms TWT measured at Horizon F, the deepest horizon analysed. The throw decreases gradually upwards, which is characteristic of blind faults or growth faults where the rate of sedimentation is larger than the rate of fault movement (Childs *et al.* 2003; Hongxing & Anderson 2007). Profile D shows a variation in throw for both F5 and F9 (Fig. 3). F5 has a maximum throw of 410 ms TWT at Horizon F, decreasing to about 210 ms upward at Horizon E. The throw increases again to about 280 ms TWT at Horizon D, and then decreases following the general trend as observed in plot C. A comparison to the throw profile of F9 shows an unexpected throw decrease of F5 at Horizon E, which correlates with the maximum throw at F9. This is interpreted as the initiation time of F9. The initiation of Fault 9 close (less than 2 km at the location of plot D) to the footwall of F5 might have caused strain to partition between F5 and F9, as indicated by throw minima at Horizon E of plot D (Fig. 3). The aggregate throw measurement of plot D shows an identical trend to plot C, a fault–growth pattern with the maximum at Horizon F, gradually decreasing upwards.

Plot E shows throw–depth measurements at the NW end of F10 (edge of the study area), documenting a maximum throw of 140 ms TWT at Horizon D, decreasing both upwards and downwards. Plot F was measured close to the linkage area between F10 and F5, F7 and F8, labelled as the intersection area in Figure 2. This plot shows a maximum of throw of about 670 ms TWT at Horizon E, decreasing upwards. This observation highlights the initiation time of F10 at Horizon E as a syndepositional normal fault that grew towards the NW. A comparison between plots E and F shows two different throw–depth trends for F10 from the SE (syndepositional trend) towards the NW (post-depositional trend).

Plot G shows the throw distribution at the common intersection area of faults F5, F7, F8 and F10, with 1050 ms throw at Horizon F, decreasing upwards. Plot H shows the throw on F8 in the footwall of F7, with two maxima: one at Horizon E with 390 ms throw, and another at Horizon C with 400 ms throw. In-between the two maxima, the throw decreases to about 360 ms. This pattern could either reflect that F8 initiated at the time of deposition of Horizon E, becoming inactive at Horizon D, which was then followed by an increase in fault throw at Horizon C, alternatively F8 initiated at Horizon C and grew downwards and linked to a pre-existing, deeper-seated fault (*sensu* Fazli Khani & Back 2015*b*). After deposition of Horizon C, the throw along F8 decreased.

Plots K and L show the temporal evolution of F7 close to the intersection area and at the centre of the fault, respectively. Both plots start with maximum throw at Horizon F, decreasing towards the shallower horizons, highlighting the typical syndepositional nature of this fault. At the very SE edge of the study area, F7-1 has been interpreted as a splay of F7, linking both laterally and vertically onto F7; its location at the very edge of the seismic data volume made throw–depth measurements on this fault segment impossible.

Lateral fault growth and linkage

Throw–distance plots along the strike of the studied faults can be used to highlight the lateral growth and linkage of the main bounding faults. Figure 4 shows that throw increases gradually on F3 from 100 ms TWT in the NW to its maximum of 320 ms TWT at the linkage area with F5. This coincides with a major increase in throw on F5 from 100 to 370 ms TWT. The general NW decrease in throw on F3 suggests that this fault initiated from the linkage area with F5 and propagated laterally towards the NW. The observations from throw–depth plots A and B (Fig. 3) confirm the interpretation that F3 initiated at Horizon D from the linkage area to F5 and propagated through time towards the NW. From the linkage area with F3, throw increases along the strike of F5, reaching its maximum of about 480 ms TWT before decreasing gradually towards the SE (Fig. 4). At the linkage area with F9, the throw on F5 decreases by about 110 ms TWT, remaining constant along the fault until the common linkage area with faults F7, F8 and F10. Fault 9 links orthogonally to F5 in the SW and to F10 at its NE tip, creating a triangular area in the footwall of F5 (Figs 2 & 3). The maximum throw of about 320 ms TWT occurs in the central part of the fault (Fig. 4). Throw on F10 increases towards the SE into the common intersection area. At the linkage area with F9, the throw on F10 increases from 150 ms TWT to about 450 ms TWT. This occurs over a short distance (a few hundreds of metres), and throw–depth plots E and F (Fig. 3) suggest that the SE segments of F10 and F9 initiated at Horizon E and accommodated significant strain, while the NW segment of F10 initiated later at Horizon D.

The cumulative throw of F5, F9 and F10 (see the aggregate curve in Fig. 4) shows a gradual increase in the SE direction towards the common intersection area. At the intersection area, where F5, F10, F8 and F7 link, throw on the aggregate curve increases to 800 ms TWT. Eastwards along F8, throw increases from 320 ms TWT at the intersection area to about 400 ms TWT at the limit of the study area. We have no seismic data beyond this point, but the continuation of F8 with depth (Fig. 2, sections C and D) suggests that it initiated in the footwall of F7 and later propagated laterally towards the common fault intersection. F7 finally has about 600 ms TWT of throw close to the common intersection area, decreasing laterally towards the SE. F7-1 links up with F7 in the very SE of the study area. Throw increases along segment F7-1 from the linkage area in the NW towards the SE.

The throw–distance plots of Figure 4 shows an overall convex shape with the maximum amount of throw localized at and around the common fault intersection, decreasing both towards the NW and SE. This suggests that, although strain migrated from one fault or a fault segment to neighbouring faults or fault segments, the aggregate amount of throw shows a throw–distance pattern similar to that of a single isolated fault.

Footwall backstepping of faults

The throw–depth plots (Fig. 5) along F7 (plots K, L and M), F8 (plot H) and at the common fault intersection (plot G) show the influence of F8 on the lateral distribution of throw along F7. The throw–depth plots along F7 all show a tripartite vertical zonation of the fault into: (1) a lower part between Horizon F and Horizon D with a relatively steep

slope related to the early stages of fault activity; (2) a transition interval (indicated in grey in Fig. 5) that is characterized by a shallow slope; and (3) a top interval with an almost vertical slope indicating decreased fault activity before cessation. In the NW (plot G), the transition interval starts at Horizon D and ends at Horizon B; in the SE (plots L and M), the transition interval lies between Horizon D and Horizon C. Plots L and M further show that the activity of F7 decreases earlier in the SE (Horizon C) than in the NW (Horizon B). These observations suggest that the initiation of F8 in the footwall of F7 caused a migration of strain through time towards the east in the SE and central part of F7. Towards the NW, the influence of fault F8 on the kinematics of F7 decreases as it approaches and links to F7 (plots K and G: Fig. 5).

Lateral fault linkage and relay zones

An integration of throw–depth plots (Figs 3 & 5), time-thickness maps between each pair of interpreted horizons (Fig. 6) (see Fazli Khani & Back 2012, 2015*b* for further discussion) and throw–distance plots (Fig. 4) highlights the temporal and spatial evolution of the main bounding faults. The throw–depth and throw–distance plots for F5 and F7 suggest that the triangular area between F5, F9 and F10 (Fig. 2) most probably originated as a relay zone between F5 and F7, and that, during propagation of these faults towards each other, F5 rotated eastwards approaching F7 (Fig. 6, Unit EF) and finally linking to F7 at the common fault intersection (Fig. 6), while F7 continued to propagate towards the NW. Fault F5 and F7 seem to act differently in the relay zone, where F5 turns into its footwall area and links onto the laterally growing F7, again, in the footwall area, and F7 continues its lateral propagation towards the NW. Following further fault activity and increase in displacement, F9 probably initiated as a connecting fault branch line (Peacock & Sanderson 1994; Long & Imber 2012) between F5 and F7 after deposition of Horizon E (Fig. 6, Unit ED), which can explain the unusual NE–SW strike of F9. Fault F10, which is most likely to be a NW continuation of F7, continued its lateral propagation after the initiation of F9, and probably terminated immediately outside the study area. Fault 5, in turn, linked to F7 and stopped its lateral propagation in the fault intersection area.

The throw–depth plot D (Fig. 3) at the location of the relay zone shows the relative activity and initiation time of F5 and F9. Fault F5 shows a general decrease in throw from Horizon F upwards. At Horizon E, where F9 initiates, the throw on F5 decreases rapidly from 410 ms TWT (Horizon F) to about 210 ms TWT (Horizon E), followed by an increase to 290 ms TWT at Horizon D. In the same interval, F9 records about 500 ms TWT of throw at the nucleation point (Horizon E), which decreases to approximately 320 ms TWT at Horizon D. This observation suggests that, in the location of the relay zone, the total amount of strain prior to the initiation of F9 was accommodated by F5; after the initiation of F9, the strain was partitioned between the two neighbouring faults. The dotted curve on the throw–depth plot D in Figure 3 shows the aggregate throw on F5 and F9 in the location of the relay zone. A comparison of the aggregate curve with plot C shows a similar throw distribution along the strike of F5. Figure 7 summarizes the lateral growth pattern of F5 and F7, and the evolution of the relay zone in their linkage area.

Rollover anticlines

A major, kilometre-scale rollover complex with associated crestal-collapse faults is located in the hanging wall of bounding faults F4, F5, F6 and F7 in the central part of the study area (Fig. 8). In total, more than 100 minor crestal-collapse faults were mapped in the rollover structure, of which most strike NW–SE, with some minor east–west strike directions. The maximum length of these synthetic and antithetic collapse faults ranges between a few hundreds of metres up to 6 km. Table 2 summarizes the main characteristics of the studied rollover complex, which exhibits, upon close inspection, five individual collapse zones (RO1– RO5 on Fig. 8). The vertical seismic reflection sections of Figure 2 show the spatial relationship between synthetic and antithetic collapse faults and the major listric bounding faults. Based on the dip direction, the crestal-collapse faults can be subdivided into two groups: SW-dipping faults (green in Fig. 8) and NE-dipping faults (violet in Fig. 8). Local graben areas are observed where a synthetic and an antithetic fault face one another (blue polygons in Fig. 8). In contrast, where two adjacent faults dip away from one another, a horst initiates in the footwall (orange polygons in Fig. 8). Based on the vertical geometry of synthetic and antithetic faults, and their map view organization of Figure 8, five distinct rollover collapses can be identified in the central study area (Figs 8 & 9). Each collapse system is characterized by a series of oppositely dipping normal faults defining a central (crestal) graben, with horst structures separating neighbouring rollover anticlines.

Rollover 1 is the most basinwards located in the hanging wall of the deep-seated FX, and dies out between Horizon E and Horizon F (Fig. 2). The collapse faults of Rollover 1 strike NW–SE (Fig. 8). Rollover 2 is located in the hanging wall of F5 close to the SE tip of F4. The SW-dipping internal

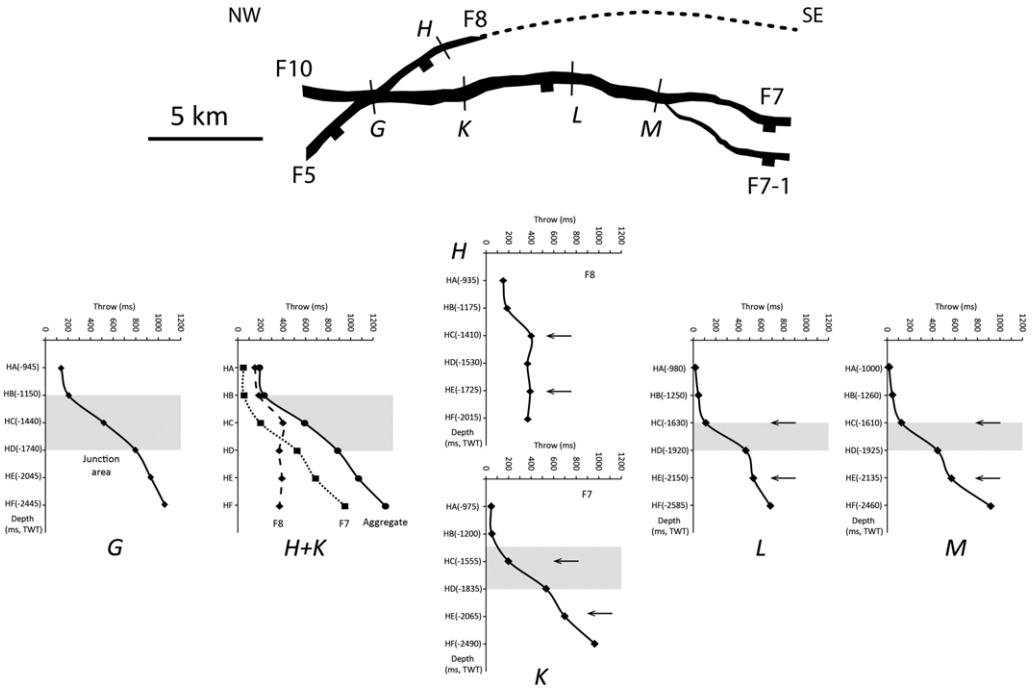

Fig. 5. Comparison of fault activity periods along the strike of F7 and the influence of F8 in the footwall of this fault. Arrows on graphs H and K show two throw maxima on F8 at Horizon E and Horizon C that correspond with a decrease in throw on F7. The grey box shows the transition between higher fault activity during the early stages and lesser fault activity in the later stages of fault growth. Towards the NW in profiles G and H + K, the transition is gradual and lasts longer compared to the SE, as profiles L and M show. A rapid decrease in fault throw in profiles L and M is due to the activity and throw maxima of F8. The influence of F8 on F7 decreases towards the NW where they link. The vertical scale in brackets is the mid-point between the hanging-wall and footwall cut-offs.

collapse faults of Rollover 2 generally strike NW–SE, while the NE-dipping collapse faults mainly strike east–west (Fig. 8). The vertical seismic-reflection section B of Figure 2 shows Rollover 3 at shallower depths, and Rollover 1 in the deeper parts of the section. The seismic section reveals the spatial relationship between a deep-seated FX and the shallower F6, F5 and F9 (see Fazli Khani & Back 2015*b* for more discussion on the geometry and linkage of deep-seated faults FX and FZ). Rollover 3 accommodates the deformation in the hanging wall of F5, F6 and F7 in the relay zone. This structure displaces strata down to Horizon F (Table 2); towards the SW, Rollover 3 is bound by the NW-dipping FY (Fig. 2, section B). Fault FY separates Rollover 3 from Rollover 1, terminating laterally in the NW within Rollover 2.

Rollovers 4 and 5 are located on the SE edge of the study area, in the hanging wall of F6, F7 and F8. On the time–structural map of Horizon D (Fig. 2a), at the location of section C, F8 is beyond the NE extent of the seismic cube. In the deeper part of the section, F8 is in the footwall of F7. Synkinematic horizons to Rollover 4 are sediments developed prior to Horizon C (Table 2). For Rollover 5, synkinematic horizons are between Horizon F and Horizon A. The following discussion focuses on delineating the relationship between the development of the major bounding faults and rollover tectonics.

Discussion

Previous interpretation and modelling studies on growth faults and rollovers (Ellis & McClay 1988; Vendeville & Cobbold 1988; McClay 1990; Mauduit & Brun 1998; Xiao & Suppe 1992; Withjack *et al.* 1995; Hodgetts *et al.* 2001; Imber *et al.* 2003; Back *et al.* 2006; Fazli Khani & Back 2015*a*) have addressed factors controlling the geometry and the development of rollovers, such as the geometry of the bounding faults, variable sedimentation rates, the amount of extension after synkinematic units are deposited and compaction. Fazli Khani & Back (2012) have shown, on the same data as used in this

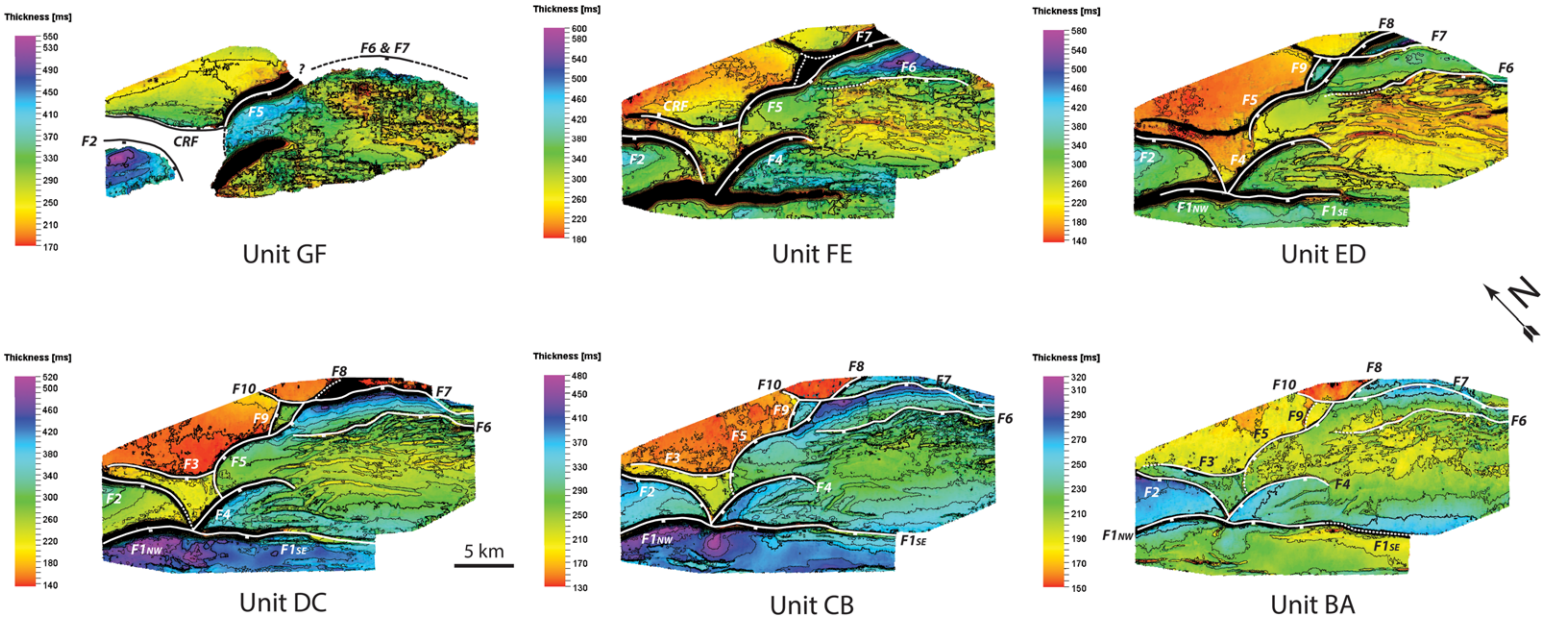

Fig. 6. Time–thickness maps showing temporal evolution of major regional faults and a counter regional fault (CRF) in the study area. The dashed lines highlight the inactive segment of the fault, while solid line shows the active segment of fault.

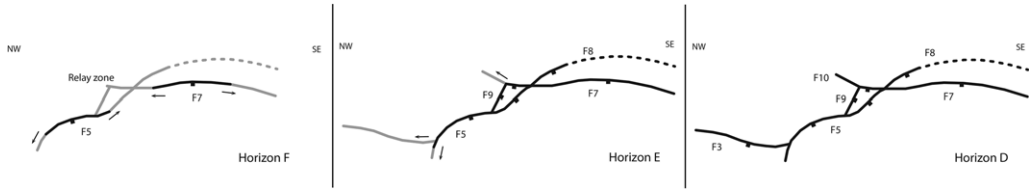

Fig. 7. Lateral and temporal evolution of the studied fault array, showing the relative initiation time and growth of faults at horizons F, E and D, and the development of the relay zone. This construction is based on the time–thickness maps and fault analysis presented here. Grey shows an inactive fault segment and black shows an active fault segment.

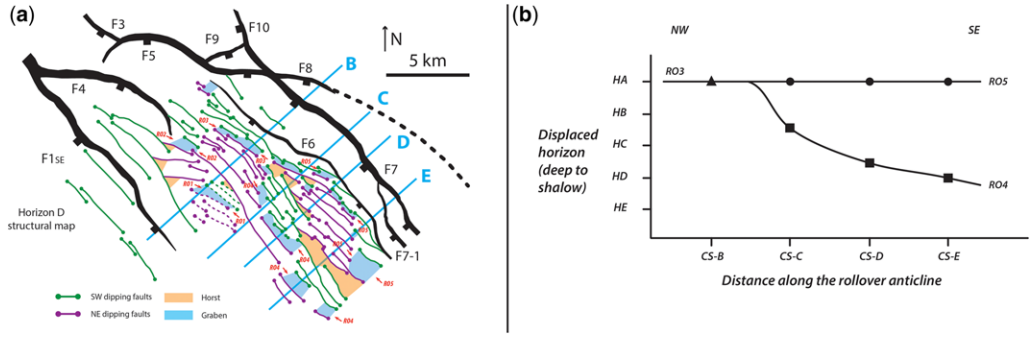

Fig. 8. (**a**) Horizon D structural map showing the main bounding faults and hanging-wall synthetic, dipping towards the SW (in green), and antithetic, dipping towards NE (in violet), normal faults. Graben and horsts are shown by blue and orange polygons, respectively. Local graben are parallel the axis of associated rollovers (hinge of the rollover anticline). Based on the orientation and location of local graben in map view, we have identified five rollover anticlines in the study area labelled RO1–RO5. (**b**) Rollover activity graph showing the shallowest horizon displaced by rollovers RO3, RO4 and RO5 along four cross–sections (CS-B, CS-C, CS-D and CS-E; see the structural map in (a) for the location of the cross-sections) along the strike of rollovers from NW to SE. Rollover 4 displaces younger intervals (between horizons B and C) in the NW, while in the SE only intervals below Horizon D have been displaced by Rollover 4 (see the text for the discussion). See the vertical cross-sections in Figure 2 for the relative activity timing of rollovers RO3, RO4 and RO5.

Table 2. *Identified rollovers and their characteristics*

Rollover name	Strike	Total number of mapped faults	Fault length (km)	Displaced horizons	Location
Rollover 1 (RO1)	NW–SE in the north and east–west in the south	20	1–3	HG to HA	Hanging wall of F5 at the eastern tip of F4
Rollover 2 (RO2)	NW–SE	32	1–5	HF to HA	Hanging wall of F5, F6 and F7, at the junction and in the relay zone area
Rollover 3 (RO3)	NW–SE	10	1–3	HG and deeper to HF	At the southern edge of the study area
Rollover 4 (RO4)	NW–SE with minor WNW–ESE	31	1–5	HF to HA and younger	Hanging wall of faults F6, F7 and F7-1
Rollover 5 (RO5)	NW–SE	28	1–6	HG and deeper to HD	SE of Rollover 4

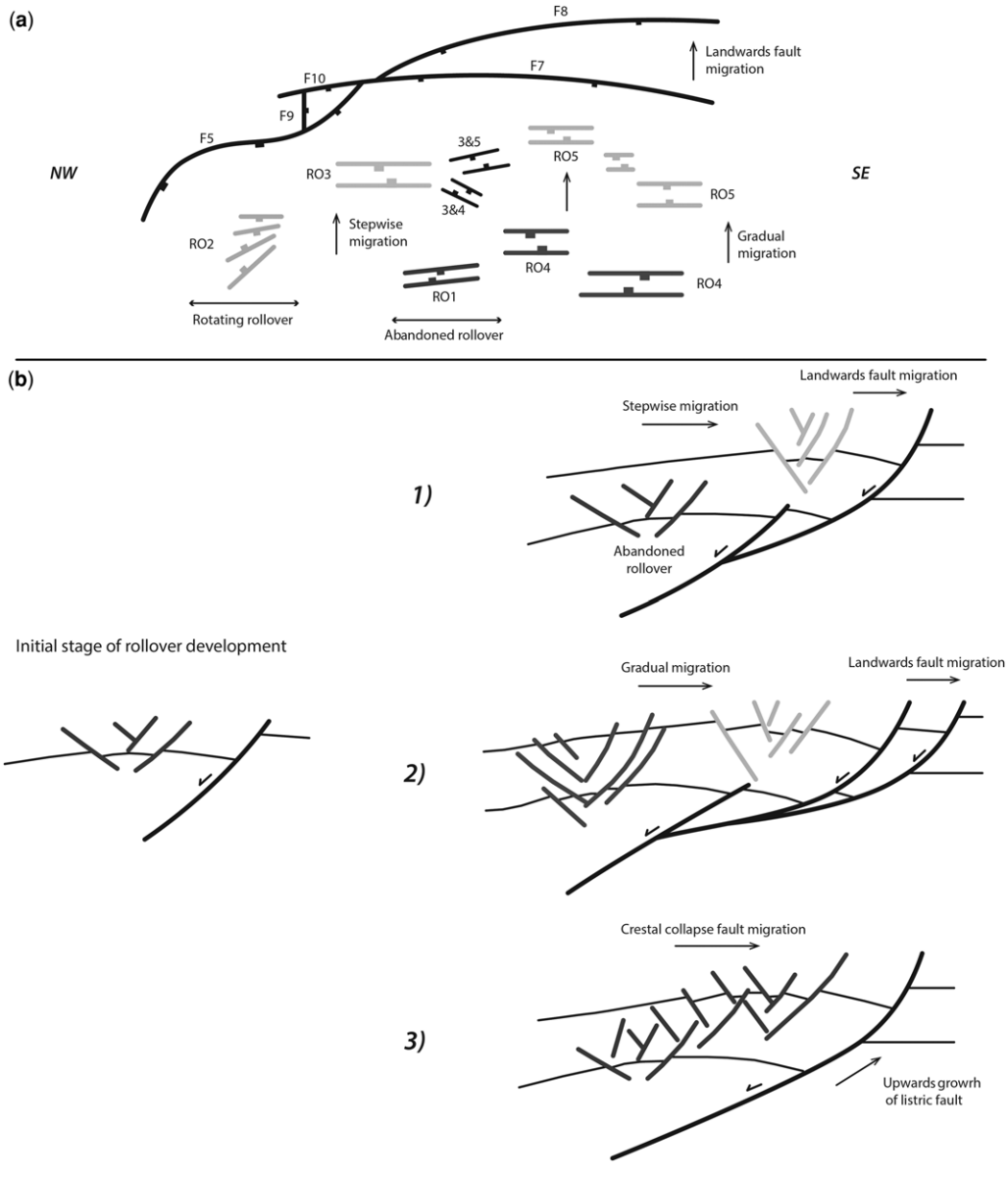

Fig. 9. Simplified schematic diagram showing the influence of normal fault growth and linkage on the evolution of hanging-wall rollover anticlines. (**a**) Map view of bounding faults and associated rollovers, showing the rotation of crestal-collapse faults in the hanging wall of fault F5 described as a fault–rollover interaction Type 1. (**b**) Three different responses of rollover anticline to their bounding-fault evolution. Type 2: the initiation of a new listric fault in the footwall of an older fault creates a new rollover anticline, while the older rollover becomes 'abandoned' with no or a little overlap in the crestal-collapse fault's activity. In this case, there is a stepwise rollover migration. Type 3: landwards migration of the bounding fault following by significant contemporaneous crestal-collapse fault activity and a more gradual migration of rollovers. Type 4: landwards migration of crestal-collapse faults within the rollover anticline due to the upwards growth and listric geometry of the bounding fault.

study in the central part of the study area, a general landwards migration of rollovers; yet, the affects of lateral (plan-view) changes in bounding-fault geometry on rollover development, including those of multiple laterally linking bounding faults that are associated with individual rollovers, have

not previously been documented. The studied part of the Niger Delta that is characterized by five individual rollover–crestal-collapse systems controlled by dynamically evolving bounding faults is an ideal example to demonstrate such effects.

The consequences of the lateral growth of a bounding fault that changes strike during its development can be best documented along F5. F5 propagated laterally to the NW and west (Figs 6 & 7) before terminating at F4 (Fig. 6). The crestal-collapse faults in the associated Rollover 2 trend NW–SE in the north, but seem to rotate with time to an east–west orientation in the south (Figs 2 & 8). The rotation of extensional collapse faults ('oblique faults' in fig. 8 of Fazli Khani & Back 2012) is most likely to be due to the change in the strike direction of F5 towards the west at its NW tip. This change probably modified the local stress field, reflected by the eas–west strike of the crestal-collapse faults in Rollover 2 (Fig. 9a, Type 1). With F5 joining F4 during the deposition of Unit DC (Fig. 6), several younger NW–SE-orientated faults in the hanging wall of F4 intersected the east–west-orientated collapse faults, creating a complex mosaic of rhomb-shaped fault-bound microblocks (Fig. 8).

An example of the along-strike influence of linking bounding faults on rollover development can be seen between the landwards faults F7 and F8 in the east of the study area. The activity of F8 in the footwall of F7 decreased the slip on F7 (Figs 3 & 4) from the NW, where the two faults link, towards the SE. The variation in lateral throw along F7 and F8 controlled the hanging-wall deformation in different ways: in the location of the relay zone and the linkage point of F7 and F8, a single rollover (RO3) accommodated the hanging-wall deformation (Fig. 2, section B; Fig. 8). Towards the SE, however, the further landwards migration of F8 (assuming that F8 continues upwards with the same dip as F7) broadened the associated hanging-wall bending, resulting in a gradual shift in crestal deformation from Rollover 4 to Rollover 5 (Fig. 2, sections C, D & E). The lateral differences in the interaction between F7 and F8 can also be seen on the throw–distance plot of Figure 4, which shows a decreasing throw for F7 towards the SE, whilst the throw of F8 increases. Although the SE portion of F8 is out of the study area, continuous faulting activity along F8 can be interpreted from the development of Rollover 5, which displaces Horizon A and even shallower and younger units irrespective of the decreasing slip along F7 (Fig. 2 sections C, D & E; Figs 3 & 5).

It should be noted that faulting in the relay zone involving faults F5, F7, F8, F9 and F10 (Figs 2, 3 & 7) resulted in the development of a single rollover (RO3), as opposed to the two rollover systems (Rollover 4 and Rollover 5) in the hanging wall of faults F6, F7 and F8. This documents that hanging-wall deformation related to several nearby faults can be accommodated by a single rollover–crestal-collapse fault system that seems somewhat unaffected by the presence of multiple interacting bounding faults and fault segments of partly different orientation. In turn, the dynamic development of several large, more-or-less sub-parallel faults at distances of >3 km (F6, F7 and F8) seems to support rollover migration following the stepwise activation of the respective main fault.

Imber *et al.* (2003) demonstrated two different responses of hanging-wall deformation to the development of a bounding fault: (1) a prolonged and progressive landwards migration of the active rollover in the hanging wall of a stationary main fault; and (2) a punctuated migration of the rollover directly related to the landwards backstepping of the main bounding fault. This study shows that deep-seated Rollover 1 (e.g. Fig. 2, section B) was most probably initiated and controlled by FX in the deeper parts of the study area, displacing Horizon G and Horizon F. This rollover became inactive prior to the deposition of Horizon E, and it is bounded by FY in the north and NW (see Fazli Khani & Back 2015*b* for detail on the evolution of FX). The subsequent development of F6, F7 and F8 in the footwall of FX seems to have initiated a new set of crestal-collapse faults (Rollover 3) on the landwards side of Rollover 1 (Fig. 2), abandoning Rollover 1 (Fig. 9b, Type 2). This contrasts with the rollover development in the SE of the study area, where Rollover 4 formed in response to the deep-seated FZ in its early stages. However, Rollover 4 continued to displace shallower horizons even after the decay of FZ (up to Horizon C: Fig. 2, section C), a time when younger F6, F7 and F8 and Rollover 5 were already active. The study area thus shows two fundamentally different responses of rollover–crestal collapse systems to the initiation of younger faults in the footwall of their original bounding faults: (1) a stepwise shift of deformation, where Rollover 1 was abandoned and Rollover 3 was initiated as new younger faults initiated in the former footwall terrain (Fig. 9b, Type 2); and (2) a more gradual shift of deformation from Rollover 4 to Rollover 5 in response to footwall collapse (Fig. 9b, Type 3). The gradual shift of rollovers with a period of contemporaneous growth of Rollover 4 and Rollover 5 is similar to the 2D sandbox experiment E44 by McClay (1990) and the systems described by Imber *et al.* (2003), and probably related to the branching of F7 and 8. In turn, the most likely reason for the complete abandonment of Rollover 1 is the limited NW extent and stratal offset of F6 (Figs 2 & 6), shifting younger rollover activity not only landwards but also laterally over a considerable distance to the SE.

A final interaction between growth faulting and rollover development documented in the study area is that synthetic and antithetic faults within a rollover structure can progressively migrate upwards and landwards without initiating a new rollover structure (see the fault pattern within RO3 in Fig. 2, section B; Fig. 9b, Type 4). A comparison with the analogue models of McClay (1990) and the northern Brunei example described by Imber *et al.* (2003) suggests that a general landwards and upwards migration of crestal-collapse faults within rollovers could be due to the upwards growth and the listric shape of a single bounding fault. However, if a secondary fault initiates in the footwall, a new rollover structure can initiate landwards, possibly laterally offset from the pre-existing rollover. This mechanism seems to require a certain distance between the original and the new bounding fault, which can be estimated for the study area to be >3 km, as well as a stratal offset at the new fault exceeding 100 ms TWT (*c.* 100 m).

Conclusions

This study shows how growth-fault characteristics can change along strike as they become influenced by the initiation and growth of neighbouring faults. The stepping of a main fault system can modify the throw distribution along its individual fault branches in the early stages of growth, reaching equilibrium in the later stages of fault growth.

The initiation and growth of rollovers is directly controlled by the kinematics of their bounding normal faults. It is shown that the lateral linkage and backstepping of bounding-fault systems can be mirrored in their associated rollover hanging walls. Based on the data presented in this study, we have identified four genetic types of fault–rollover interaction, including: (1) the rotation of a rollover–crestal-collapse system, which is controlled by changing lateral bounding-fault orientation during fault growth; (2) a stepwise shift of rollover–crestal-collapse systems associated with rollover abandonment, controlled by the initiation of a new fault in the footwall of an older structure; (3) a gradual migration of successive rollovers controlled by branching, connected fault systems; and (4) a general landwards and upwards migration of crestal-collapse faults within individual rollovers above listric, upwards-growing, stationary main faults.

This study finally shows that bounding faults and their associated rollovers can dynamically interact, and that an overlap in the timing of rollover activity is likely to depend on the distance, connectivity and lateral (plan-view) arrangement and geometry of the bounding faults.

We thank the Shell Petroleum Development Company of Nigeria for providing the seismic data presented in this study. Schlumberger is gratefully acknowledged for providing Petrel under an academic user license agreement. Paul Whipp, an anonymous reviewer and volume editor Conrad Childs are thanked for their constructive comments on the earlier version of the manuscript. This study is a contribution to Project Ba 2136/4-1 funded by the Deutsche Forschungsgemeinschaft (DFG).

References

Back, S. & Morley, C. 2016. Growth faults above shale – Seismic-scale outcrop analogues from the Makran foreland, SW Pakistan. *Marine and Petroleum Geology*, **70**, 144–162.

Back, S., Tioe, H.J., Thang, T.X. & Morley, C.K. 2005. Stratigraphic development of synkinematic deposits in a large growth-fault system, onshore Brunei Darussalam. *Journal of the Geological Society, London*, **162**, 243–258, https://doi.org/10.1144/0016-764903-006

Back, S., Höcker, C., Brundiers, M.B. & Kukla, P.A. 2006. Three-dimensional-seismic coherency signature of Niger Delta growth faults: integrating sedimentology and tectonics. *Basin Research*, **18**, 323–337.

Back, S., Strozyk, F., Kukla, P.A. & Lambiase, J.J. 2008. 3D restoration of original sedimentary geometries in deformed basin fill, onshore Brunei Darussalam, NW Borneo. *Basin Research*, **20**, 99–117.

Baudon, C. & Cartwright, J. 2008. The kinematics of reactivation of normal faults using high resolution throw mapping. *Journal of Structural Geology*, **30**, 1072–1084.

Beach, A. & Trayner, P. 1991. The geometry of normal faults in a sector of the offshore Nile Delta, Egypt. *In*: Roberts, A.M., Yielding, G. & Freeman, B. (eds) *The Geometry of Normal Faults*. Geological Society, London, Special Publications, **56**, 173–182, https://doi.org/10.1144/GSL.SP.1991.056.01.11

Brown, L.F., Jr., Loucks, R.G., Trevino, R.H. & Hammes, U. 2004. Understanding growth-faulted, intraslope subbasins by applying sequence-stratigraphic principles: examples from the south Texas Oligocene Frio Formation. *American Association of Petroleum Geologists Bulletin*, **88**, 1501–1522.

Bruce, C. 1973. Shale tectonics, Texas coastal area growth faults. *In*: Bally, A.W. (ed.) *Seismic Expression of Structural Styles*. American Association of Petroleum Geologists, Studies in Geology, **15**, 878–886.

Burke, K.C.B. 1972. Longshore drift, submarine canyon, and submarine fans. *American Association of Petroleum Geologists Bulletin*, **56**, 1975–1983.

Cartwright, J.A., Bouroullec, R., James, D. & Johnson, H.D. 1998. Polycyclic motion history of Gulf Coast Growth Faults from high resolution kinematic analysis. *Geology*, **26**, 819–822.

Childs, C., Nicol, A., Walsh, J.J. & Watterson, J. 2003. The growth and propagation of synsedimentary faults. *Journal of Structural Geology*, **25**, 633–648.

Damuth, J.E. 1994. Neogene gravity tectonics and depositional processes on the deep Niger Delta continental margin. *Marine and Petroleum Geology*, **11**, 321–346.

Dooley, T., Ferguson, A., Poblet, J. & McClay, K. 2000. Tectonic evolution of the Sanga Sanga Block, Mahakam Delta, Kalimantan, Indonesia. *American Association of Petroleum Geologists Bulletin*, **84**, 765–786.

Doust, H. 1990. Petroleum Geology of the Niger Delta. *In*: Brooks, J. (ed.) *Classic Petroleum Provinces*. Geological Society, London, Special Publications, **50**, 365–380, https://doi.org/10.1144/GSL.SP.1990.050.01.21

Doust, H. & Omatsola, E. 1989. Niger Delta. *In*: Edwards, J.D. & Santogrossi, P.A. (eds) *Divergent/Passive Margins*. American Association of Petroleum Geologists, Memoirs, **48**, 201–238.

Duffy, O.B., Bell, R.E., Jackson, C.A.-L., Gawthorpe, R.L. & Whipp, P.S. 2015. Fault growth and interactions in a multiphase rift fault network: Horda Platform, Norwegian North Sea. *Journal of Structural Geology*, **80**, 99–119.

Dula, W.F. 1991. Geometric models of listric normal faults and rollover folds. *American Association of Petroleum Geologists Bulletin*, **75**, 1609–1625.

Edwards, M.B. 1976. Growth faults in Upper Triassic deltaic sediments, Svalbard. *American Association of Petroleum Geologists Bulletin*, **60**, 341–355.

Ellis, P.G. & McClay, K.R. 1988. Listric extensional fault systems – results of analogue model experiments. *Basin Research*, **1**, 55–70.

Evamy, B.D., Haremboure, J., Kamerling, P., Knaap, W.A., Molloy, F.A. & Rowlands, P.H. 1978. Hydrocarbon habitat of Tertiary Niger Delta. *American Association of Petroleum Geologists Bulletin*, **62**, 277–298.

Fairhead, J.D. & Binks, R.M. 1991. Differential opening of the Central and South Atlantic oceans and the opening of the West African rift system. *Tectonophysics*, **187**, 191–203.

Fazli Khani, H. & Back, S. 2012. Temporal and lateral variation in the development of growth faults and growth strata in the western Niger Delta, Nigeria. *American Association of Petroleum Geologists Bulletin*, **96**, 595–614.

Fazli Khani, H. & Back, S. 2015*a*. The influence of differential sedimentary loading on rollover and accommodation creation in deltas. *Marine and Petroleum Geology*, **59**, 136–149.

Fazli Khani, H. & Back, S. 2015*b*. The influence of preexisting structure on the growth of syn-sedimentary normal faults in a deltaic setting, Niger Delta. *Journal of Structural Geology*, **73**, 18–32.

Fossen, H. & Rotevatn, A. 2016. Fault linkage and relay structures in extensional settings – A review. *Earth-Science Reviews*, **154**, 14–28.

Gawthorpe, R.L. & Leeder, M.R. 2000. Tectono-sedimentary evolution of active extensional basins. *Basin Research*, **12**, 195–218.

Gibbs, A.D. 1984. Structural evolution of extensional basin margins. *Journal of the Geological Society, London*, **141**, 609–620, https://doi.org/10.1144/gsjgs.141.4.0609

Hodgetts, D., Imber, J. *et al.* 2001. Sequence stratigraphic responses to shoreline-perpendicular growth faulting in shallow marine reservoirs of the champion field, offshore Brunei Darussalam, South China Sea. *American Association of Petroleum Geologists Bulletin*, **85**, 433–457.

Hongxing, G. & Anderson, J.K. 2007. Fault throw profile and kinematics of normal fault: conceptual models and geologic examples. *Geological Journal of China Universities*, **13**, 75–88.

Hooper, R.J., Fitzsimmons, R.J., Grant, N. & Vendeville, B.C. 2002. The role of deformation in controlling depositional patterns in the south-central Niger Delta, West Africa. *Journal of Structural Geology*, **24**, 847–859.

Imber, J., Childs, C., Nell, A.R., Walsh, J.J., Hodgetts, D. & Flint, S. 2003. Hanging wall fault kinematics and footwall collapse in listric growth fault systems. *Journal of Structural Geology*, **25**, 197–208.

Ings, S.J. & Beaumont, C. 2010. Continental margin shale tectonics: preliminary results from coupled fluid-mechanical models of large-scale delta instability. *Journal of the Geological Society, London*, **167**, 571–582, https://doi.org/10.1144/0016-76492009-052

Jackson, C.A.-L. & Rotevatn, A. 2013. 3D seismic analysis of the structure and evolution of a salt-influenced normal fault zone: a test of competing fault growth models. *Journal of Structural Geology*, **54**, 215–234.

Long, J.J. & Imber, J. 2012. Strain compatibility and fault linkage in relay zones on normal faults. *Journal of Structural Geology*, **36**, 16–26.

Lopez, J.A. 1990. Structural styles of growth faults in the U.S. Gulf Coast Basin. *In*: Brooks, F. (ed.) *Classic Petroleum Provinces*. Geological Society, London, Special Publications, **50**, 203–219, https://doi.org/10.1144/GSL.SP.1990.050.01.10

Lowell, J.D. 1985. *Structural Styles in Petroleum Exploration*. OGCI Publications, Tulsa, OK.

Marten, R., Shann, M., Mika, J., Rothe, S. & Quist, Y. 2004. Seismic challenges of developing the pre-Pliocene Akhen Field offshore Nile Delta. *The Leading Edge*, **23**, 314–320.

Mauduit, T. & Brun, J. 1998. Growth fault/rollover systems: birth, growth, and decay. *Journal of Geophysical Research*, **103**, 18,119–18,136.

McClay, K.R. 1990. Extensional fault systems in sedimentary basins: a review of analogue model studies. *Marine and Petroleum Geology*, **7**, 206–233.

McCulloh, R. 1988. Differential fault-related early Miocene sedimentation, Bayou Herbert area, southwestern Louisiana. *American Association of Petroleum Geologists Bulletin*, **72**, 477–492.

Morley, C.K. & Guerin, G. 1996. Comparison of gravity-driven deformation styles and behavior associated with mobile shales and salt. *Tectonics*, **15**, 1154–1170.

Morley, C.K., Back, S., Van Rensbergen, P., Crevello, P. & Lambiase, J.J. 2003. Characteristics of repeated, detached, Miocene–Pliocene tectonic inversion events in a large delta province on an active margin, Brunei Darussalam, Borneo. *Journal of Structural Geology*, **25**, 1147–1169.

Onuoha, K.M. 1999. Structural features of Nigeria's coastal margin: an assessment base of age data from wells. *Journal of African Earth Sciences*, **29**, 485–499.

Peacock, D.C.P. & Sanderson, D.J. 1991. Displacements, segment linkage and relay ramps in normal fault zones. *Journal of Structural Geology*, **13**, 721–733.

Peacock, D.P.C. & Sanderson, D.J. 1994. Geometry and development of relay ramps in normal fault systems.

American Association of Petroleum Geologists Bulletin, **78**, 147–165.

POCHAT, S., CASTELLTORT, S., CHOBLET, G. & DRIESSCHE, J.V.D. 2009. High-resolution record of tectonic and sedimentary processes in growth strata. *Marine and Petroleum Geology*, **26**, 1350–1364.

ROUBY, D. & COBBOLD, P.R. 1996. Kinematic analysis of a growth fault system in the Niger Delta from restoration in map view. *Marine and Petroleum Geology*, **13**, 565–580.

SALLER, A. & BLAKE, G. 2003. Sequence stratigraphy and syndepositional tectonics of Upper Miocene and Pliocene deltaic sediments, offshore Brunei Darussalam. *In*: SIDI, F.H., NUMMEDAL, D., IMBERT, P., DARMAN, H. & POSAMENTIER, H.W. (eds) *Tropical Deltas of Southeast Asia – Sedimentology, Stratigraphy, and Petroleum Geology*. Society for Sedimentary Geology (SEPM), Special Publications, **76**, 219–234.

SANDAL, S.T. 1996. *The Geology and Hydrocarbon Resources of Negara Brunei Darussalam*. Brunei Museum, Bandar Seri Begawan, Brunei.

SAPIN, F., RINGENBACH, J.-C., RIVES, T. & PUBELLIER, M. 2012. Counter-regional normal faults in shale-dominated deltas: origin, mechanism and evolution. *Marine and Petroleum Geology*, **37**, 121–128.

SESTINI, G. 1989. Nile Delta, a review of depositional environments and geological history. *In*: WHATELEY, M.K.G. & PICKERING, K.T. (eds) *Deltas, Sites and Traps for Fossils Fuels*. Geological Society, London, Special Publications, **41**, 99–127, https://doi.org/10.1144/GSL.SP.1989.041.01.09

SHEN, Z., DAWERS, N.H., TÖRNQVIST, T.E., GASPARINI, N.M., HIJMA, M.P. & MAUZ, B. 2016. Mechanisms of late Quaternary fault throw-rate variability along the north central Gulf of Mexico coast: implications for coastal subsidence. *Basin Research*, first published online February 23, 2016, https://doi.org/10.1111/bre.12184

SHORT, K.C. & STAEUBLE, A.J. 1967. Outline of geology of Niger delta. *American Association of Petroleum Geologists Bulletin*, **51**, 761–779.

TAYLOR, S.K., NICOL, A. & WALSH, J.J. 2008. Displacement loss on growth faults due to sediment compaction. *Journal of Structural Geology*, **30**, 394–405.

THORSEN, C.E. 1963. Age of growth faulting in southeast Louisiana. *Gulf Coast Association of Geological Societies Transactions*, **13**, 103–110.

VAN RENSBERGEN, P. & MORLEY, C. 2000. 3-D seismic study of a shale expulsion syncline at the base of the Champion Delta, offshore Brunei, and its implications for the early structural evolution of large delta systems. *Marine and Petroleum Geology*, **17**, 861–872.

VENDEVILLE, B. & COBBOLD, P.R. 1988. How normal faulting and sedimentation interact to produce listric faut profiles and stratigraphic wedges. *Journal of Structural Geology*, **10**, 649–659.

WHITE, N.J., JACKSON, J.A. & MCKENZIE, D.P. 1986. The relationship between the geometry of normal faults and that of the sedimentary layers in their hangingwalls. *Journal of Structural Geology*, **8**, 897–909.

WHITEMAN, A.J. 1982. *Nigeria: Its Petroleum Geology, Resources and Potential, Volume 1*. Graham Trotman, London.

WITHJACK, M.O. & SCHLISCHE, R.W. 2006. Geometric and experimental models of extensional fault-bend folds. *In*: BUITER, S.J.H. & SCHREURS, G. (eds) *Analogue and Numerical Modelling of Crustal-scale Processes*. Geological Society, London, Special Publications, **253**, 285–305, https://doi.org/10.1144/GSL.SP.2006.253.01.15

WITHJACK, M.O., ISLAM, Q.T. & POINTE, P.R. 1995. Normal faults and their hanging-wall deformation: an experimental study. *American Association of Petroleum Geologists Bulletin*, **79**, 1–18.

XIAO, H. & SUPPE, J. 1992. Origin of rollover. *American Association of Petroleum Geologists Bulletin*, **76**, 509–529.